X-ray Crystallographic and Analytical Ultracentrifugation Analyses of Truncated and Full-Length Yeast Copper Chaperones for SOD (LYS7): A Dimer−Dimer Model of LYS7−SOD Association and Copper Delivery[†,‡]

Leslie T. Hall,[§] Raylene J. Sanchez,[‖] Stephen P. Holloway,[§] Haining Zhu,[‖] Jennifer E. Stine,[§] Thomas J. Lyons,[‖] Borries Demeler,[⊥] Virgil Schirf,[⊥] Jeffrey C. Hansen,[⊥] Aram M. Nersissian,[‖] Joan Selverstone Valentine,[‖] and P. John Hart*,[§]

Center for Biomolecular Structure Analysis and Center for Analytical Ultracentrifugation of Macromolecular Assemblies, Department of Biochemistry, University of Texas Health Science Center at San Antonio, 7703 Floyd Curl Drive, San Antonio, Texas 78284-7760, and Department of Chemistry and Biochemistry, University of California, Los Angeles, California 90095

ABSTRACT: Copper−zinc superoxide dismutase (CuZnSOD) acquires its catalytic copper ion through interaction with another polypeptide termed the copper chaperone for SOD. Here, we combine X-ray crystallographic and analytical ultracentrifugation methods to characterize rigorously both truncated and full-length forms of apo-LYS7, the yeast copper chaperone for SOD. The 1.55 Å crystal structure of LYS7 domain 2 alone (L7D2) was determined by multiple-isomorphous replacement (MIR) methods. The monomeric structure reveals an eight-stranded Greek key β-barrel similar to that found in yeast CuZnSOD, but it is substantially elongated at one end where the loop regions of the β-barrel come together to bind a calcium ion. In agreement with the crystal structure, sedimentation velocity experiments indicate that L7D2 is monomeric in solution under all conditions and concentrations that were tested. In contrast, sedimentation velocity and sedimentation equilibrium experiments show that full-length apo-LYS7 exists in a monomer−dimer equilibrium under nonreducing conditions. This equilibrium is shifted toward the dimer by approximately 1 order of magnitude in the presence of phosphate anion. Although the basis for the specificity of the LYS7−SOD interaction as well as the exact mechanism of copper insertion into SOD is unknown, it has been suggested that a monomer of LYS7 and a monomer of SOD may associate to form a heterodimer via L7D2. The data presented here, however, taken together with previously published crystallographic and analytical gel filtration data on full-length LYS7, suggest an alternative model wherein a dimer of LYS7 interacts with a dimer of yeast CuZnSOD. The advantages of the dimer−dimer model over the heterodimer model are enumerated.

Copper is required for the activation of dioxygen, which is essential for the survival of all living aerobic organisms (*1*). Paradoxically, the electronic structure of copper that allows its direct interaction with oxygen also renders it quite toxic. Cells therefore tightly regulate the amount of copper allowed into the cytoplasm (*2*). In addition, cells are armed with a variety of proteins, e.g., the metallothioneins, that scavenge free copper ions. Proteins that use copper ion as a cofactor must somehow acquire it in the face of these scavenging molecules. Knowledge of how this occurs has increased substantially in the last several years with the discovery of a class of molecules termed "copper chaperones" (*3*). The copper chaperones acquire copper either directly or indirectly from the membrane transporter CTR1, protect it from the scavenging molecules (and the cellular environment from it), and deliver and insert it into specific target proteins, thereby activating them (reviewed in ref *4*).

In eukaryotes, several copper chaperones have been identified, including Cox17, which delivers copper to cytochrome *c* oxidase in the mitochondria (*5, 6*), Atx1, which delivers copper to vesicular transport ATPases such as Ccc2 (*7, 8*), and CCS and LYS7, which deliver copper to cytoplasmic human and yeast copper−zinc superoxide dismutase, respectively (*3*). These copper-bearing proteins are highly specific for their targets and cannot functionally substitute for each other in their respective pathways (*3*).

Single-site mutations in CuZnSOD[1] cause the neurodegenerative disease familial amyotrophic lateral sclerosis (FALS), the inherited form of Lou Gehrig's disease (*9*). A copper-mediated toxic gain of function in FALS mutant CuZnSODs may play a role in motor neuron death (*10, 11*).

Thus, focus on the copper chaperone for copper–zinc superoxide dismutase has intensified, and it may be a potential target for novel therapeutic avenues to combat the disease. The importance of the copper chaperone for SOD in CuZnSOD function is underscored by in vivo studies showing that LYS7 knockout yeast display oxygen sensitivity and produce copper-free SOD at normal polypeptide levels (*12*). Either LYS7 or CCS supplied in trans in these LYS7 knockout yeast rescues the oxygen sensitive phenotype and restores the biosynthesis of holo-SOD1 (*3*).

CCS and LYS7 each have three domains. N-Terminal domain 1 is comprised of approximately 80 amino acid residues which contain a putative copper binding consensus sequence (MXCXXC) found in the copper-transporting ATPases (*13*, *14*) and in the cytosolic copper chaperone Atx1 (*7*, *15*). The structures of both apo-Atx1 and Hg–Atx1 are known (*16*) and consist of an overall ferrodoxin-like $\beta\alpha\beta\beta\alpha\beta$ fold. The metal binding MXCXXC motif is on a solvent-exposed loop in the Atx1 molecule, and the cysteine residues in this motif are found to coordinate Hg(II) in a linear fashion in the Hg–Atx1 structure (*16*). Hg(II) presumably mimics Cu(I) binding to Atx1; however, all Cu–Atx1 structures examined thus far display disordered metal-binding loops, and the copper ion is not visible (*16*). In the apo-Atx1 structure, the two cysteines of this motif form a disulfide bond accompanied by a rearrangement of the flexible loop, where one of the cysteine residues (Cys15) moves approximately 4 Å (*16*). Domains 2 of the copper chaperones for SOD are "SOD-like". Human CCS domain 2 is 47% identical to human CuZnSOD, a similarity which extends to the residues that are involved in metal binding and in the formation of the SOD dimer interface (*3*, *17*). In contrast, domain 2 of yeast LYS7 is only 26% identical to yeast CuZnSOD and by sequence alignment appears to have lost the amino acid residues responsible for metal binding. Domain 3 of CCS and LYS7 is only slightly homologous to other known proteins but contains a CXC motif absolutely required to copper-metalate and thereby activate copper-free SOD (*18*).

Recent biochemical and homology modeling studies have suggested a mechanism of copper delivery to SOD wherein domain 1 recruits cellular copper, domain 2 facilitates target recognition, and domain 3 mediates copper insertion into apo-SOD (*18*, *19*). The X-ray crystal structure of the full-length apo-LYS7 protein was recently reported (*20*). In the crystal, the two SOD-like domains (domain 2) of LYS7 interact to form a dimer with a subunit interface similar to that found in the SOD1 homodimer, suggesting that LYS7–SOD recognition may involve formation of a LYS7–SOD heterodimer. A model of the hypothetical LYS7–SOD heterodimer generated by superimposing domain 2 of the LYS7 structure onto a monomer of yeast SOD reveals no critical steric interference between interface residues (*20*). Unfor-

tunately, domain 3 of the protein was disordered in the structure and could not be visualized. Schmidt et al. subsequently reported that apo-LYS7 exists as a monomer in gel filtration studies under physiological conditions at all concentrations that were analyzed (100–750 μM, corresponding to ∼2.7–20 mg/mL) (*18*). Thus, the oligomeric state of apo-LYS7 in solution remains unresolved.

To investigate these issues further, we pursued X-ray crystallographic studies on LYS7 domain 2 alone (L7D2) (residues 78–220) in conjunction with analytical ultracentrifugation studies on both the L7D2 and full-length LYS7 molecules. Here, we present the results of these studies indicating that (1) L7D2 is monomeric both in the 1.55 Å crystal structure and in solution under all conditions tested, (2) L7D2 binds a calcium ion at the apex of its elongated β-barrel, linking three of four loops together either via direct interactions with the protein or via a network of bound water molecules, (3) monomeric full-length apo-LYS7 may have different conformations in solution depending upon the presence or absence of a reducing agent, (4) full-length apo-LYS7 in 25 mM phosphate buffer (pH 7.5) under nonreducing conditions exists in a reversible monomer–dimer equilibrium with a dissociation constant of 3.0×10^{-6} M, and (5) a dimeric model of L7D2 generated by structural alignment with the yeast SOD homodimer reveals an electropositive surface complementary to an electronegative surface on the yeast SOD homodimer. On the basis of these results, we suggest an alternative model for copper delivery from LYS7 to yeast SOD based on an interaction of a homodimer of LYS7 with a homodimer of yeast SOD.

EXPERIMENTAL PROCEDURES

Protein and Crystals. DNA fragments encoding the 249-amino acid full-length LYS7 protein and its 143-amino acid SOD-like domain 2 (L7D2) (residues Ser78–Gly220) were prepared by PCR amplification from genomic clone template DNA derived from plasmid pSL2502, kindly provided by G. F. Sprague (University of Oregon, Eugene, OR) (*21*). PCR products were subcloned into the pET-3d bacterial expression vector (Stratagene) (*22*), and were sequenced for verification of the integrity of the DNA sequences. Full-length LYS7 and L7D2 proteins were expressed in *Escherichia coli* strain BL21(DE3) under the control of the IPTG-inducible lacUV5 promoter. Cells were grown to an OD_{600} of 0.8, and expression was induced with 1 mM IPTG. Expression continued for 6 h, and cells were harvested and disrupted by sonication. SDS–PAGE analysis indicated that both full-length LYS7 and L7D2 were present in soluble fractions as well as in inclusion bodies. The proteins from soluble fractions were purified in the presence of EDTA and DTT by a combination of anion exchange chromatography on DEAE-cellulose (Whatman) and gel filtration chromatography on Sephadex G-75 superfine (Pharmacia). Refolding and purification of the proteins from inclusion bodies were performed according to a previously published procedure for the blue copper protein stellacyanin (*23*). The identity and purity of L7D2 and full-length LYS7 proteins, which each give a single band in 15% SDS–PAGE, were confirmed by electrospray ionization mass spectrometry. The proteins were verified to be metal-free using inductively coupled plasma mass spectrometry. L7D2 purified from inclusion bodies displays a CD spectrum identical to that recorded for the

---

[1] Abbreviations: CuZnSOD, copper–zinc superoxide dismutase; SOD, copper–zinc superoxide dismutase; SOD1, copper–zinc superoxide dismutase; ySOD, yeast copper–zinc superoxide dismutase; hSOD, human copper–zinc superoxide dismutase; hCCS, human copper chaperone for superoxide dismutase; LYS7, yeast copper chaperone for superoxide dismutase; L7D2, domain 2 of the yeast copper chaperone for superoxide dismutase; Atx1, yeast copper chaperone for Ccc2; FALS, familial amyotrophic lateral sclerosis; rms, root-mean-square; PCR, polymerase chain reaction; MIR, multiple isomorphous replacement.

protein obtained from the soluble fraction, indicating it has the correct folding topology (data not shown).

For use in crystallization trials, purified L7D2 was transferred to 20 mM Tris-HCl (pH 8.0), 1 mM EDTA, and 0.5 mM DTT and concentrated to ~50 mg/mL using a Centricon 10 spin concentrator (Amicon). The protein concentration was calculated using a molar extinction coefficient of 16 000 M^{-1} cm^{-1} at 278 nm derived from the two tryptophan and four tyrosine residues per L7D2 molecule. Crystals of L7D2 were obtained by the hanging drop vapor diffusion method. The concentrated L7D2 protein solution was mixed with varying volumes (between 2 and 5 μL) of reservoir solution (Hampton Research Crystal Screen condition 14) consisting of 100 mM Hepes (pH 7.5), 28% PEG 400, and 200 mM $CaCl_2$ and allowed to equilibrate at 4 °C. Large football- or teardrop-shaped crystals with dimensions of approximately 0.5 mm × 0.3 mm × 0.3 mm appeared within 2 weeks in space group $P2_12_12_1$ with the following unit cell parameters: $a = 34.2$ Å, $b = 46.3$ Å, and $c = 73.9$ Å; each contained one L7D2 molecule per asymmetric unit.

Heavy Atom Derivative Preparation and Data Collection. Isomorphous heavy atom derivatives were prepared by soaking suitable L7D2 crystals overnight in the dark at 4 °C in a solution obtained by mixing 5 μL of the reservoir solution made 30% in PEG 400 with 2 μL of this same solution saturated in the heavy atom compound of interest. High-resolution diffraction data from native and heavy atom derivative L7D2 crystals were collected at room temperature on a Rigaku RU-H3R rotating anode X-ray generator equipped with MSC/Yale mirrors and an R-AXIS IV imaging plate detector. Oscillation images were taken every 2°, rotating the crystals about the ϕ axis.

Structure Determination and Refinement. Putative heavy atom derivative data sets from L7D2 crystals soaked in 12 different compounds were collected, and five of them [CH_3-$Hg(C_2H_3O_2)$, K_2PtCl_4, K_2AuCl_6, K_2OsCl_6, and K_2IrCl_6] displayed self-consistent difference Patterson peaks in the $P2_12_12_1$ Harker sections. The program SOLVE (*24*) independently identified the major heavy atom sites via difference Patterson analyses, and several minor sites were located automatically via the cross difference Fourier routines in the program. Phasing and refinement of heavy atom parameters in SHARP (*25*) followed by solvent flattening and histogram matching using DM (*26*) produced readily interpretable electron density maps. Initial stages of refinement were carried out in X-PLOR (*27*), and in the final stages, SHELXL-97 (*28*) was used. R_{free} was monitored in both refinement programs using identical test reflection sets. Model adjustment used all data (no σ cutoff) during multiple rounds of crystallographic refinement. A "round" of refinement is defined as computational (least squares and/or molecular dynamics) refinement of the structure followed by visual inspection of electron density maps coupled with manual model rebuilding (when necessary), using the molecular graphics program O (*29*). Model atom positions were verified by the examination of conventional and simulated annealing omit maps (*30*). The annealed omit maps were calculated by excluding atoms found in a 6 Å radius sphere around every fifth residue in the protein sequence and by heating to 2500 K during the simulated annealing protocol. Structural alignment of L7D2 and yeast CuZnSOD backbone atoms was accomplished using a modified version of the

program ALIGN (*31*). Crystallographic figures were created with the molecular graphics programs SETOR and GRASP (*32, 33*). Atomic coordinates and diffraction data have been deposited in the Protein Data Bank with codes 1EJ8 and r1EJ8sf, respectively.

Analytical Ultracentrifugation. Sedimentation velocity and sedimentation equilibrium experiments were performed using a Beckman Optima XL-I analytical ultracentrifuge equipped with both UV absorbance and Rayleigh interference optics. Double-sector charcoal/Epon filled centerpieces were used for both sedimentation velocity and sedimentation equilibrium experiments. Sedimentation velocity runs on reduced and unreduced protein in the absence of metal ions were performed simultaneously at 20 °C using an eight-hole AN-50 rotor spinning at 48 000 rpm. Protein samples (420 μL) were made in 25 mM phosphate buffer (pH 7.5) at three concentrations (see below) in the presence or absence of 10 mM tris(2-carboxyethyl)phosphine (TCEP-HCl), a non-thiol-containing compound that reduces disulfide bonds but does not absorb at the wavelengths monitored here. Low- and medium-concentration runs were performed at 230 nm ($OD_{230} = 0.8$) and 280 nm ($OD_{280} = 0.8$), respectively, using absorbance optics. High-concentration experiments ($OD_{280} = 2.4$) were performed using interference optics. These OD values correspond to protein concentrations of 0.08−2.4 mg/mL for L7D2 and 0.07−2.2 mg/mL for full-length LYS7. The resulting sedimentation velocity data were analyzed by the method of van Holde and Weischet using the computer program UltraScan 4.1 (*34, 35*). The top and bottom 4% of each boundary were excluded from the analyses due to the high amount of experimental noise in these regions. In some cases, the sedimentation velocity runs were repeated and analyzed as described above in 5 mM Tris-HCl (pH 7.5) and 100 mM NaCl and in 100 mM NaCl alone (pI of LYS7 = 6.65). Where indicated, the scans used for the van Holde and Weischet analysis also were used to calculate the second-moment sedimentation coefficient using UltraScan 4.1.

Sedimentation equilibrium experiments were performed at 20 °C using a four-hole AN-60 rotor. Three 120 μL samples of unreduced protein in the absence of metal ions in 25 mM phosphate (pH 7.5) were loaded at an OD_{280} of 0.2, 0.25, and 0.3, and were sedimented to equilibrium at 24 000, 27 500, and 31 000 rpm. Absorbance scans at 280 nm were measured in the radial step mode at 0.001 cm intervals, and data were collected taking the average of 20 measurements at each radial distance. The program PC-NONLIN was used for global fitting of the equilibrium data (*36*). As with the velocity runs, the sedimentation equilibrium experiments were in some cases repeated in 25 mM Tris-HCl (pH 7.5) and 100 mM NaCl and in 100 mM NaCl alone.

RESULTS

Native L7D2 crystals diffract X-rays exceptionally well at room temperature, and 97.4% complete native data were collected to 1.55 Å resolution ($R_{sym} = 5.4\%$ on the measured intensities). Heavy atom derivative crystals diffract X-rays to smaller angles of θ than do crystals of the native protein and also tend to exhibit significant decay in their diffracted intensities after several hours in the X-ray beam. Isomorphous data from the mercury, platinum, osmium, iridium, and gold derivatives, together with anomalous difference information from the mercury, platinum, osmium, and
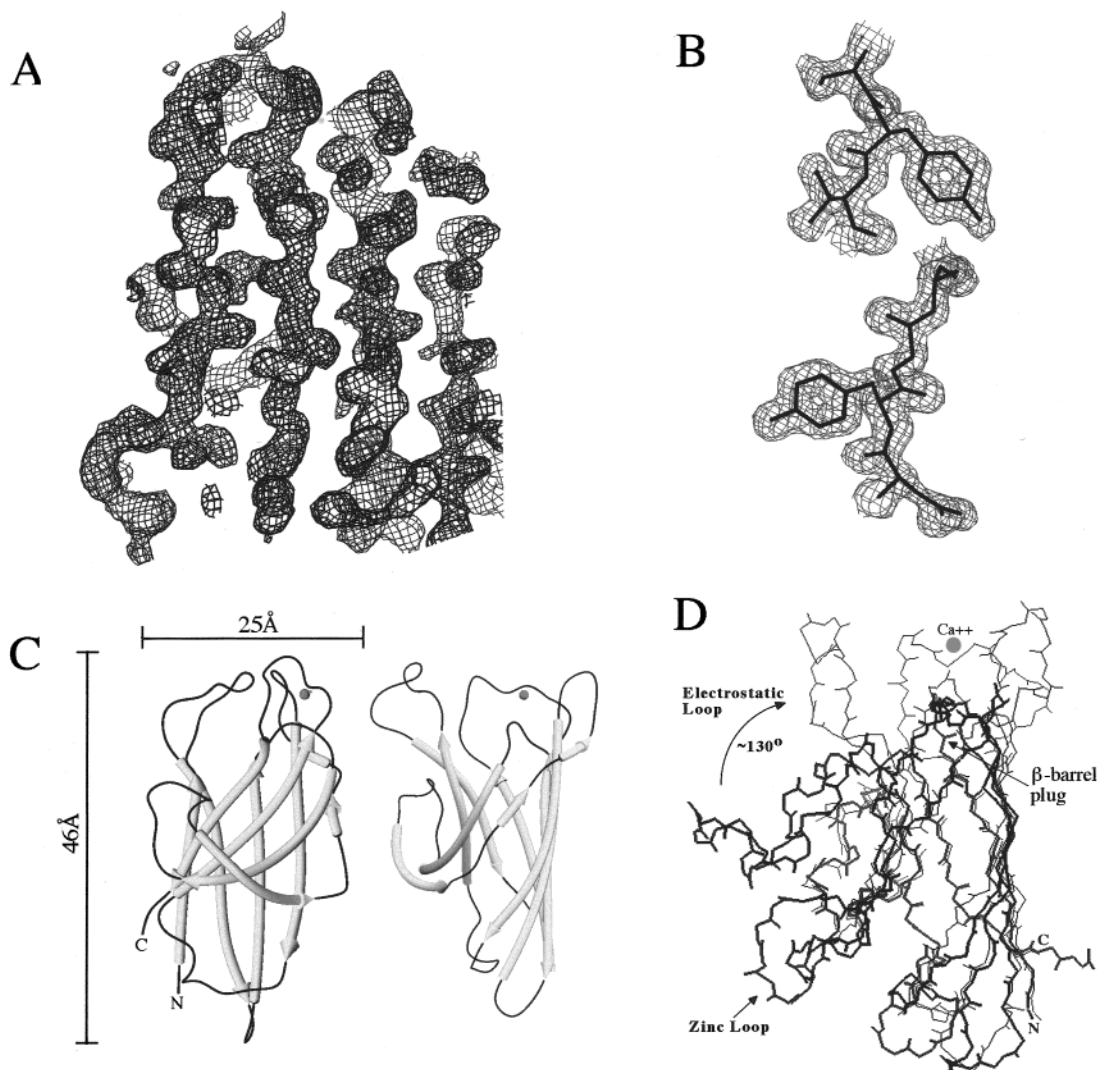
FIGURE 1: L7D2 structure determination. (A) Multiple-isomorphous replacement (MIR) experimental electron density map obtained from five heavy atom derivatives using the programs SHARP (25) and DM (26). Four strands of β-sheet run vertically in the image. (B) Final SIGMAA-weighted electron density map superimposed on Tyr129 and Tyr209. (C) Overall fold and dimensions of the molecule. The left image shows a view looking into the saddle-shaped cleft (see the text). The right image is rotated clockwise (looking from the top) in the plane of the paper approximately 90° relative to the left image. The small sphere represents the position of the bound calcium ion. (D) Superposition of the refined L7D2 molecule (thin lines) with a monomer of yeast CuZnSOD (thick lines) in the same orientation as the right image in panel C. Note that the region corresponding to the zinc loop in yeast SOD is absent in L7D2 and that the region corresponding to the electrostatic loop in yeast SOD is flipped approximately 130° into a different conformation that extends the β-barrel in L7D2. The positions of the bound calcium ion and β-barrel plug are indicated.

iridium derivatives, were used in the generation of a high-resolution multiple-isomorphous replacement map. Overall, the MIR-phased and solvent-flattened electron density maps produced with SOLVE (24) were not interpretable, although very short regions of β-sheet were visible. Subsequent phasing and refinement of heavy atom parameters in ML-PHARE (26) followed by solvent flattening and histogram matching using DM (26) failed to improve the experimental electron density maps to any appreciable extent.

In contrast, refinement of heavy atom isomorphous, anomalous, and nonisomorphism parameters in the program SHARP (25) using all available diffraction data ($\sigma > 0$) from the native and derivative data sets followed by solvent flattening and phase extension in DM resulted in a high-quality experimental electron density map, where amino acid side chains were clearly visible and large stretches of the L7D2 protein backbone could be easily traced. Figure 1A shows a representative portion of this experimental electron

density map. Systematic combination of partial model phases with the MIR phases using the routine SIGMAA (26, 37) in successive rounds of model building improved the electron density in the loop regions so the entire L7D2 molecule could be built unambiguously.

The refinement of the L7D2 structure can be summarized as follows. The final model contains 1082 protein atoms, 140 amino acid residues, 112 water molecules, and one bound calcium ion. The R-value is 19.6% (R_{free} = 25.8%) for all data from 10 to 1.55 Å where $\sigma > 0$. rms deviations from ideality for bond lengths and angles are 0.008 Å and 2.2°, respectively. No amino acid residues fall outside the allowed ϕ and φ angles in a Ramachandran plot (38). The N-terminal Met residue (an artifact of the expression system used) and the C-terminal Ser218, Ala219, and Gly220 residues were not visible in the electron density map and thus were not modeled. Amino acid residues 203−205 exhibited high thermal parameters and were somewhat

Table 1: Crystallographic Data, Phasing, and Refinement of LYS7 Domain 2[a,b]

X-ray Data						
	native	mercury	platinum	osmium	iridium	gold
no. of observations	78174	43706	43729	31507	33634	12363
no. of unique reflections	17203	8236	6947	6240	6224	3397
redundancy	4.5	5.3	6.3	5.0	5.4	3.6
resolution range (Å)	90−1.55	50−2.0	90−2.1	50−2.2	50−2.2	50−2.6
(last shell)	(1.61−1.55)	(2.07−2.00)	(2.18−2.10)	(2.28−2.20)	(2.28−2.20)	(2.69−2.60)
completeness (%)	97.4 (88.7)	98.3 (98.8)	95.9 (96.3)	98.6 (98.1)	97.7 (98.9)	85.0 (89.4)
(last shell)						
R_{sym} (on I) (%)[c]	5.4 (34.6)	8.4 (32.6)	12.7 (32.4)	6.1 (9.3)	7.9 (12.1)	12.6 (35.0)
(last shell)						
R_{iso} (%)[d]		30.5	23.1	12.9	17.9	15.6

Phasing						
		phasing power (centric/acentric)[e]				
	d_{min} (Å)	3 sites	2 sites	2 sites	2 sites	2 sites
isomorphous	5.56	1.46/1.86	1.54/2.17	3.10/3.20	1.91/2.53	1.29/1.86
anomalous		/2.55	/1.89	/1.58	/1.93	
isomorphous	3.50	0.98/1.27	0.99/1.21	1.65/1.95	1.62/1.84	0.86/1.01
anomalous		/1.57	/0.96	/1.16	/1.22	
isomorphous	2.74	0.91/1.22		1.49/2.07	1.37/1.88	
anomalous		/1.30		/1.00	/1.05	
isomorphous	2.33			1.44/1.92	1.20/1.71	

Phasing						
		R_{cullis} (centric/acentric)[f]				
	d_{min} (Å)	3 sites	2 sites	2 sites	2 sites	2 sites
isomorphous	5.56	0.69/0.68	0.74/0.68	0.66/0.62	0.70/0.64	0.84/0.86
anomalous		/0.68	/0.87	/0.90	/0.88	
isomorphous	3.50	0.85/0.87	0.90/0.90	0.77/0.74	0.82/0.80	
anomalous		/0.81	/0.88	/0.95	/0.98	
isomorphous	2.74	0.90/0.90	0.77/0.68	0.82/0.75		
anomalous		/0.85	/0.97	/0.99		
isomorphous	2.33			0.82/0.70	0.83/0.75	

Refinement			
resolution range (Å)	10−1.55	rmsd for bonds (Å)	0.008
no. of "rounds"[g]	22	rmsd for angles (deg)	2.2
R_{cryst} (%)[h]	19.6	no. of protein atoms	1082
R_{free} (%)[i]	25.8	no. of water molecules	112
$F/\sigma F$	>0	no. of metal ions	1 (calcium)

[a] The refined model and the corresponding structure factors have been deposited in the Protein Data Bank. [b] Three-dimensional diffraction data were collected using a Rigaku RAXIS IV imaging plate detector mounted on a Rigaku H3RHB (RU-300) generator with focusing mirrors running at 50 kV and 100 mA. X-ray data were reduced and processed using the programs DENZO and SCALEPACK (51). [c] $R_{sym} = \Sigma|I - \langle I \rangle|/\Sigma I$, where I is the observed intensity and $\langle I \rangle$ is the average intensity of multiple symmetry-related observations of that reflection. [d] $R_{iso} = \Sigma||F_{ph}| - |F_p||/\Sigma|F_p|$, where $|F_p|$ is the protein structure factor amplitude and $|F_{ph}|$ is the heavy atom derivative structure factor amplitude. [e] Phasing power = (rms$|F_h|$)/(rms E), where $|F_h|$ is the heavy atom structure factor amplitude and E is the residual lack of closure error. [f] $R_{cullis} = \Sigma|E|/\Sigma||F_{ph}| - |F_p||$. [g] See the text for the definition. [h] $R_{cryst} = \Sigma||F_p^{obs}| - |F_p^{calc}||/\Sigma|F_p^{obs}|$. [i] $R_{free} = \Sigma||F_p^{obs}| - |F_p^{calc}||/\Sigma|F_p^{obs}|$, where $|F_p^{obs}|$ is from a test set not used in the structural refinement (10% of the observed data). Crystal-to-detector distance = 100 mm. Temperature = 20 °C. Oscillation range = 2°.

disordered. Ser204, Ser205, and Arg217 had weak electron density and were modeled as glycine. Diffraction data, phasing, and refinement statistics for the L7D2 structure determination are shown in Table 1. Panels B and C of Figure 1 show a representative portion of the SIGMAA-weighted electron density map superimposed on a portion of the refined model and the overall fold and dimensions of the L7D2 molecule. Figure 1D shows a superposition of the refined L7D2 molecule and a monomer of yeast CuZnSOD (39). L7D2 and yeast CuZnSOD align with a rmsd of 1.5 Å for 405 main chain target pairs.

To determine the solution-state properties of reduced and unreduced L7D2 and full-length LYS7, sedimentation velocity runs were performed in 25 mM phosphate buffer (pH 7.5) in the absence of metal ions and the resulting scans analyzed by the method of van Holde and Weischet (34) to obtain the integral distribution of sedimentation coefficients, $G(s)$. Sedimentation data are summarized in Table 2. Figure 2A demonstrates that L7D2 sedimented as a single 1.6−1.7 S species under all conditions that were studied, as indicated by the vertical $G(s)$ plots (35). In contrast, under reducing conditions (i.e., in the presence of TCEP-HCl), full-length LYS7 sedimented as a single ∼2.3 S species at low (△), medium (□), and high concentrations (○) (Figure 2B). Interestingly, in the absence of a reducing agent and at low concentrations (▲), the full-length LYS7 protein sedimented as a 2.4−2.5 S species. The small difference in S between the reduced and unreduced forms of full-length LYS7 at low concentrations observed in the $G(s)$ plots (Figure 2B inset) also was clearly apparent when the same boundaries were used to calculate the second-moment sedimentation coefficient for these proteins (Figure 2C). Finally, analysis of unreduced LYS7 at medium (■) and high concentrations (●) yielded a substantially right-shifted $G(s)$ plot having the

Table 2: Sedimentation Velocity Analyses of Apo-L7D2 and Full-Length Apo-LYS7 Proteins[a]

	L7D2 low[b]	L7D2 high[b]	L7D2 low[b]	L7D2 high[b]	LYS7 low[b]	LYS7 medium[b]	LYS7 high[b]	LYS7 low[b]	LYS7 medium[b]	LYS7 high[b]
oxidation state[c]	reduced	reduced	unreduced	unreduced	reduced	reduced	reduced	unreduced	unreduced	unreduced
OD_{280}	n/d	2.4	n/d	2.4	n/d	0.8	2.4	n/d	0.8	2.4
OD_{230}	0.8	n/d	0.8	n/d	0.8	n/d	n/d	0.8	n/d	n/d
protein concentration (mg/mL)	0.08	2.40	0.08	2.40	0.07	0.74	2.20	0.07	0.74	2.20
S_{vhw}[d]	1.65	1.65	1.65	1.65	2.30	2.30	2.30	2.45	3.20[f]	3.20[f]
S_{SM}[e]					2.30			2.44		

[a] All protein samples were in 25 mM phosphate buffer (pH 7.5). [b] Low, medium, and high concentrations were made as described in the text. [c] Reduced protein samples contained 10 mM tris(2-carboxyethyl)phosphine (TCEP-HCl). [d] Average $s_{20,w}$ derived from fraction = 50% of the integral distribution plot (Figure 2). Except where indicated, all samples were homogeneous (see the text). [e] Second-moment $s_{20,w}$. [f] Heterogeneous sample ranging from 2.2 to 3.6 S.

characteristic shape expected for a self-associating system (*35*). When the same samples of concentrated unreduced protein were subsequently diluted to low concentrations (∗ and +, respectively), the ∼2.4 S species again predominated. Taken together, the sedimentation velocity data suggest both that unreduced full-length LYS7 exists in solution in a reversible monomer−*n*-mer equilibrium and that the reduced and unreduced forms of the full-length LYS7 monomer may have subtly different conformations. Sedimentation velocity experiments performed in Tris-HCl (pH 7.5) and 100 mM NaCl and in 100 mM NaCl alone gave results very similar to those found in the phosphate-buffered system (data not shown).

To determine rigorously the details of the monomer−*n*-mer equilibrium behavior revealed by the sedimentation velocity experiments, the unreduced full-length LYS7 protein was analyzed by sedimentation equilibrium (Figure 3). Nine data sets obtained by sedimenting three different loading concentrations to equilibrium at three different speeds in 25 mM phosphate buffer (pH 7.5) were fit globally using the program PC-NONLIN (*36*). The best fit was obtained with a monomer−dimer equilibrium model, which resulted in a variance of 3×10^{-5} with 1365 degrees of freedom. The monomer−dimer equilibrium constant was found to be 3.38 $\times 10^5$ M^{-1} (95% confidence limits from 2.27×10^5 to 5.04×10^5 M^{-1}), which corresponds to a dissociation constant of 3.0×10^{-6} M. The monomer molecular mass was determined to be 27 760 Da (95% confidence intervals from 26 749 to 28 774 Da). This value agrees extremely well with the actual molecular mass calculated from the amino acid sequence (27 322 Da).

Sedimentation equilibrium data of unreduced full-length LYS7 protein samples obtained without phosphate anion in (a) 5 mM Tris-HCl (pH 7.5) and 100 mM NaCl and (b) in 100 mM NaCl alone were also globally fit to a monomer−dimer equilibrium model. In 5 mM Tris-HCl (pH 7.5) and 100 mM NaCl, the monomer−dimer equilibrium constant was determined to be 9.08×10^4 M^{-1} (95% confidence limits from 6.06×10^4 to 1.35×10^5 M^{-1}) corresponding to a dissociation constant of 1.1×10^{-5} M. In 100 mM NaCl, the monomer−dimer equilibrium constant was determined to be 4.97×10^4 M^{-1} (95% confidence limits from 3.43×10^4 to 7.09×10^4 M^{-1}) corresponding to a dissociation constant of 2.0×10^{-5} M.

DISCUSSION

X-ray Structure of L7D2. L7D2 is a flattened eight-stranded Greek key β-barrel with dimensions of 46 Å × 25 Å × 16 Å. Figure 1C shows that the elongated, disk-shaped molecule has one very flat surface opposed by a saddle-shaped cleft on the other side of the molecule. As expected from a protein whose sequence is 26% identical with that of yeast SOD, the overall topology of the Greek key β-barrel fold is conserved. The L7D2 monomer structurally aligns with a monomer of yeast SOD with a rms deviation of 1.5 Å for 407 backbone atom target pairs. Figure 1D shows a superposition of the structure of L7D2 with that of a monomer of yeast SOD determined at 1.7 Å resolution (*39*).

The major differences in the two structures are as follows. (a) Residues 64−81 in yeast SOD corresponding to the "zinc loop" and containing zinc ligands His71 and His80 are deleted in L7D2. (b) The loop formed by residues 122−143 in ySOD, known as the "electrostatic loop" or the "active site lid loop" (*40*), is shortened and in a completely different conformation (rotated about 130°) in L7D2 (Figure 1D). This different conformation, coupled with the loss of the zinc loop, is instrumental in the formation of the saddle shape seen in Figure 1C as well as in the formation of a β-barrel in L7D2 that is significantly elongated (∼13 Å) relative to ySOD. (c) The apolar interactions that form the β-barrel "plug" in all known CuZnSODs (*41*, *42*) are replaced in L7D2 by a series of completely new interactions which are predominantly electrostatic, hydrogen bonded, and water-mediated. (d) In L7D2, a calcium ion is coordinated at the apex of this elongated β-barrel, linking three of the four loops together either via direct interactions with the protein (Ca^{2+}−O124, Ca^{2+}−O168, and Ca^{2+}−OD1−168) or via a network of bound water molecules, some of which are calcium ion ligands themselves (Figure 4). (e) The concave surface of the saddle found in L7D2 is lined with serine, glutamic acid, and aspartic acid residues. The rim of the saddle is ringed by histidine and positively charged lysine residues, features suggesting a surface that could conceivably interact with another protein.

In contrast to the monomeric structure of L7D2 reported here, full-length LYS7 displays a domain 2-mediated dimer in the asymmetric unit (*20*). The full-length LYS7 dimer interface resembles that of yeast SOD in overall size and buried surface area, and approximately 64% of the residues at the LYS7 dimer interface are conserved with respect to yeast SOD (*20*, *39*). Notable differences between the full-length LYS7 and yeast SOD interfaces, however, include the substitution of charged residues in LYS7 (Lys136 and Arg217) for hydrophobic residues in yeast SOD (Phe50 and Leu151). These two substitutions translate into four local
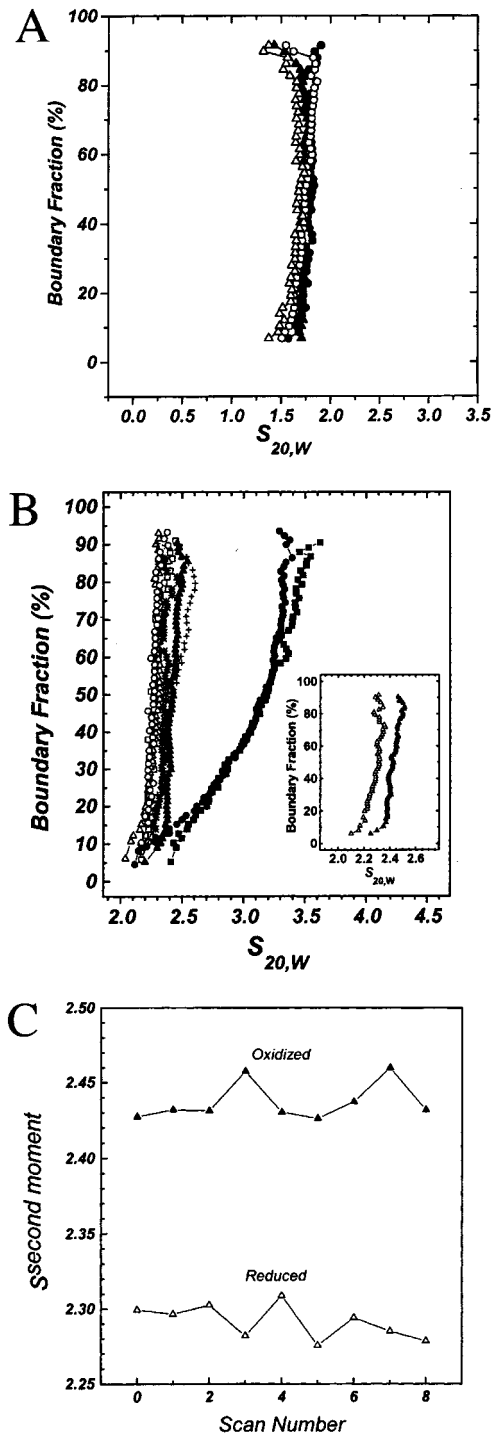
FIGURE 2: Sedimentation velocity analysis of apo-L7D2 and full-length apo-LYS7 in 25 mM phosphate buffer (pH 7.5). (A) $G(s)$ plots of L7D2 obtained after analysis of the boundaries by the method of van Holde and Weischet (*34*). Reduced $OD_{230} = 0.8$ (△). Reduced $OD_{280} = 2.4$ (○). Oxidized $OD_{230} = 0.8$ (▲). Oxidized $OD_{280} = 2.4$ (●). (B) $G(s)$ plots of full-length LYS7. Reduced OD_{230} = 0.8 (△). Reduced $OD_{280} = 0.8$ (□). Reduced $OD_{280} = 2.4$ (○). Oxidized $OD_{230} = 0.8$ (▲). Oxidized $OD_{280} = 0.8$ (■). Oxidized $OD_{280} = 2.4$ (●) (see the text). The inset shows only the $G(s)$ distributions corresponding to the reduced (△) and oxidized (▲) protein at $OD_{230} = 0.8$. (C) For the reduced (△) and oxidized (▲) protein at $OD_{230} = 0.8$, the scans used to obtain the $G(s)$ plots were analyzed to obtain the second-moment sedimentation coefficient ($s^{second\ moment}$) and results plotted as $s^{second\ moment}$ vs scan number.

three-dimensional changes due to the 2-fold symmetry at the dimer interface, and dramatically alter the electrostatic
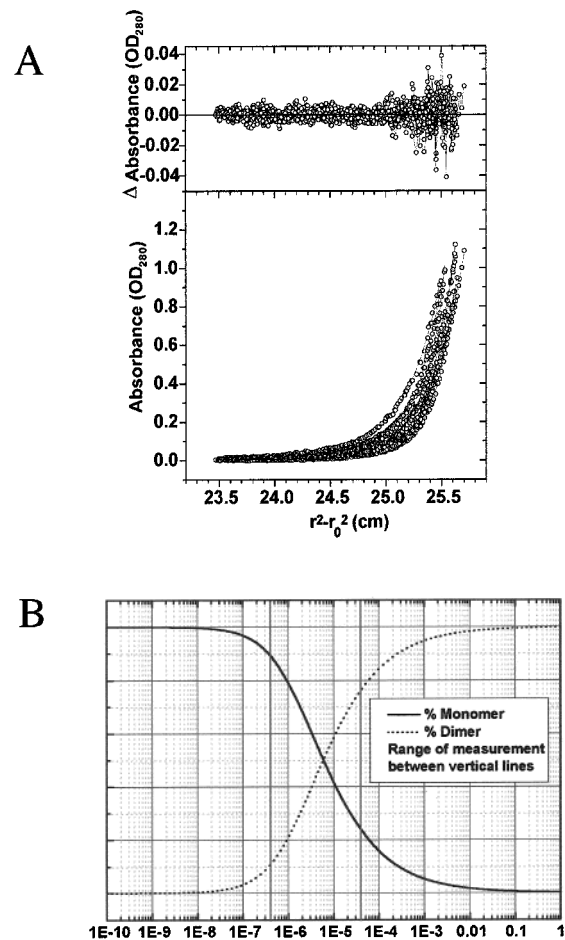

FIGURE 3: Sedimentation equilibrium analysis of full-length apo-LYS7 in 25 mM phosphate buffer (pH 7.5). (A) Samples were sedimented to equilibrium as described in Experimental Procedures, and the resulting data sets were globally fit to a monomer−dimer equilibrium model using the program PC-NONLIN (*36*). The lower panel shows the fits to the raw data, while the residuals are shown in the upper panel. Details of the fit are described in the text. (B) Plot of the relative concentration (in %) of the full-length LYS7 monomer and dimer as a function of LYS7 molar concentration as derived from the equilibrium constant measured as described for panel A.

character of this region relative to that of yeast SOD (see below).

Lamb et al. (*20*) suggest that the full-length LYS7 dimer interface may be destabilized, relative to yeast SOD, by the substitution of these positively charged residues for their hydrophobic counterparts. This hypothesis is supported by the observation that the substitution of Phe50 with glutamic acid in human SOD results in the formation of a stable monomer (*43*). The putative electrostatic destabilization of the full-length LYS7 dimer due to these basic amino acid substitutions appears, however, to be offset by the presence of two sulfate ions that are bound by dimer-related (2-fold molecular symmetry-related) Lys136, Arg188, and Arg217 side chains, and the gain of two hydrogen bonds from the interaction of the dimer-related NE2 atoms of Arg217 and their dimer-related carbonyl oxygen atoms of Ile186 (*20*). Panels b and d of Figure 4 in Lamb et al. show that the C-terminal loop residues of domain 1 that connect to the N-terminal residues of domain 2 at the dimer interface in full-length LYS7 come very close to this sulfate ion and its binding site. It remains unclear, however, whether main chain
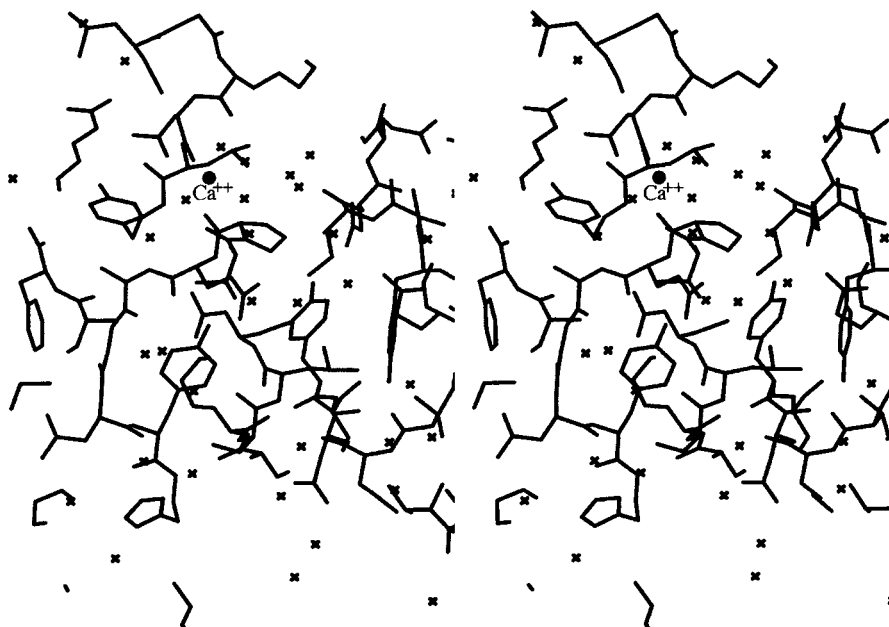
FIGURE 4: Calcium ion binding site in L7D2. The calcium ion is represented as a black sphere and is labeled. Water molecules are represented by small crosses. Note the calcium ion and water molecule-mediated hydrogen bonding network and the electrostatic interactions that link the loops together at this elongated end of the L7D2 β-barrel (see the text).

or side chain residues from this connecting loop region also interact with sulfate ion in the crystal structure, further stabilizing the full-length LYS7 homodimer (*20*). On the basis of these observations, the binding of two sulfate ions at the symmetrical LYS7 dimer interface introduces as few as six and as many as eight new hydrogen bonding interactions that may assist in the tethering of the two SOD-like domain subunits together. These observations further suggest that the presence of sulfate or phosphate ion (the latter of which is fairly abundant in the cytoplasm) could be significant in facilitating full-length LYS7 dimer formation in vivo (see below).

The structure of L7D2 differs from domain 2 of the full-length LYS7 molecule in that the C-terminal residues Ser218, Ala219, and Gly220 are not visible in our electron density map and are therefore not modeled. Arg217, an amino acid that coordinates sulfate ion in full-length LYS7 (*20*), does not display visible electron density for its side chain and is thus modeled as glycine. The resulting loss of two hydrogen bonds (dimer-related Arg217 NE2···Ile186 O), the fact that L7D2 crystals are grown in the absence of sulfate or phosphate ions, the disorder of three C-terminal L7D2 residues, and, in particular, the absence of domains 1 and 3 all may influence the L7D2 oligomeric state and dictate that it be monomeric. In support of this hypothesis, L7D2 appears to be monomeric in solution under all conditions that were tested in analytical ultracentrifugation experiments, even in the presence of phosphate ion (see the next section). Ultimately, the details of the differences between L7D2 and full-length LYS7 domain 2 structures and the development of a structure-based rationale as to why they exist in different oligomeric states in the crystal (and in solution, see below) await direct comparison of their atomic coordinates. In particular, regions corresponding to the dimer interface in full-length LYS7, the effect domains 1 and 3 have on these interface regions, and the calcium ion binding site in L7D2 should be examined closely in this context.

Solution-State Behavior of L7D2 and Full-Length LYS7. To probe the molecular basis for the differences in the oligomeric states observed in the two independently determined crystal structures (ref *20* and this study), we performed analytical sedimentation velocity and sedimentation equilibrium experiments with both apo-L7D2 and full-length apo-LYS7 proteins. Extremely important features of analytical ultracentrifugation experiments are that they are performed in standard aqueous solutions (in the absence of any solid matrix that might interact with the protein of interest, e.g., during gel filtration) and that the sample is visualized in real time during sedimentation, which allows very accurate determination of hydrodynamic and thermodynamic parameters of macromolecules in their native state under biologically relevant solution conditions (*44*, *45*).

Figure 2A shows the integral distribution of *S* plots of four sedimentation velocity runs on the apo-L7D2 molecule in 25 mM phosphate buffer (pH 7.5) under different concentrations and oxidation states. L7D2 sediments as a single ~1.7 S species in the presence or absence of reducing agent and regardless of the protein concentration. Because the full-length LYS7 monomer sediments at ~2.3 S (Figure 2B), these results strongly suggest that L7D2 is a monomer in solution. Thus, the oligomeric states of L7D2 as determined by X-ray crystallography and sedimentation velocity are in strong agreement. Importantly, domains 1 and 3 of LYS7 are likely to play a significant role in dimer formation via allosteric interactions, and their absence in L7D2 might dictate that it be a monomer under all concentrations and buffer conditions (see below).

Figure 2B shows the integral distribution of *S* plots of the full-length LYS7 apoprotein at different concentrations, and in the presence and absence of a reducing agent in 25 mM phosphate buffer (pH 7.5). As with L7D2, under reducing conditions and at all concentrations, full-length LYS7 exists as a monomeric ~2.3 S species. Without a reducing agent, however, sedimentation equilibrium data have established

that full-length LYS7 exists in a reversible monomer−dimer equilibrium with a dissociation constant of 3.0×10^{-6} M (Figure 3). The global fit to this reversible monomer−dimer equilibrium model is excellent, as indicated by the random residuals and a variance of 3×10^{-5} with 1365 degrees of freedom. Dilution of concentrated unreduced samples causes full-length LYS7 dimers to dissociate into monomers, indicating that dimer formation is mediated via noncovalent interactions. Similar results are obtained in the absence of phosphate ion, although the association constant is decreased by approximately 1 order of magnitude. A structural basis for this observed shift in the equilibrium toward the dimer in the presence of phosphate anion is described in the above section and in ref 20.

These results are consistent with previously reported gel filtration data on apo-LYS7 only if these gel filtration experiments were undertaken in the presence of a reducing agent (18). The fact that the presence of a reducing agent inhibits dimer formation in solution, even at high protein concentrations, is significant in light of the fact that the only disulfide bond known to exist in the full-length apo-LYS7 structure exists between Cys17 and Cys20 residues within domain 1, the Atx1-like domain (20). Due to steric and geometric constraints, it is unlikely that a disulfide bond can form between the two cysteine residues in the CXC motif of domain 3 (19, 46). In any case, it is difficult to envision how disruption of a localized disulfide bond within either domain 1 or domain 3 could affect the oligomeric state of the full-length LYS7 protein.

The fact that we observe full-length apo-LYS7 in a reversible monomer−dimer equilibrium under nonreducing conditions in the analytical ultracentrifuge and that Schmidt et al. (18) observe predominantly dimeric full-length LYS7 under reducing conditions in gel filtration experiments when LYS7 is copper-loaded suggests that the unreduced apo-LYS7 three-dimensional conformation may mimic that of the metal-loaded conformation. In the metalated full-length LYS7 molecule, the cysteine residues of the Atx1-like domain (Cys17 and Cys20) and those of the CXC motif in domain 3 (Cys229 and Cys231) can simultaneously coordinate copper, bringing domains 1 and 3 into proximity (see Figures 5 and 6). When domains 1 and 3 are tethered via copper binding, they themselves may participate in dimer formation, or exert subtle conformational changes on the residues found at the heart of the dimer interface that are directly connected to these domains, thus making them competent for dimer formation.

An "allosteric conformational change" that facilitates dimerization of the unmetalated, nonreduced full-length apo-LYS7 molecule could occur if interdomain disulfide bonds were to form between Cys17 and/or Cys20 in domain 1 and Cys229 and/or Cys231 in domain 3. Reduction of the putative interdomain disulfide bonds (with TCEP in our studies) could mimic the loss of copper and result in allosteric changes that preclude dimer formation. In support of this hypothesis, careful inspection of $G(s)$ plots in Figure 2B indicates that the presence of reducing agent alters the S value of the reduced full-length LYS7 monomer by ~0.15 S across the entire distribution relative to that of the unreduced LYS7 monomer (Figure 2B inset). Furthermore, when the same data used to obtain the $G(s)$ plots were analyzed by the second-moment method (Figure 2C), reduced and unreduced
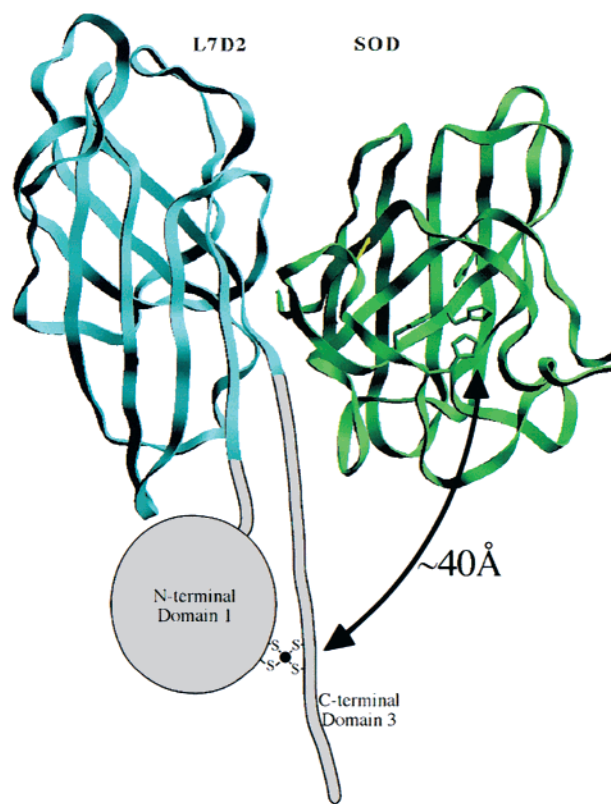

FIGURE 5: Heterodimer model of LYS7−SOD interaction and copper ion transfer. L7D2 is in blue, and yeast SOD is in green. Domains 1 (N-terminal) and 3 (C-terminal) of LYS7 are represented as a stylized circle and an extended tail, respectively. The position of the copper binding site in yeast SOD is indicated by the four histidine ligands represented by green tubes. Note the long distance the C-terminal domain must move to deposit copper into yeast SOD via this model (see the text).

full-length LYS7 at a protein concentration of 0.07 mg/mL $(OD_{230} = 0.8)$ yielded second-moment S values of 2.30 ± 0.01 and 2.44 ± 0.01 (standard deviation), respectively. The larger S value for the unreduced full-length monomer relative to that of the reduced full-length monomer is most simply explained by a more compact shape and therefore decreased frictional coefficient, consistent with a redox-dependent conformational change. The type of metal- or oxidation-based "allosteric switch" described here is attractive because SOD1 is present in many-fold excess over LYS7 (47, 48). After copper delivery to apo-SOD, the loss of metal may trigger allosteric changes that disfavor LYS7 homodimer or heterodimer formation with SOD, and could allow LYS7 to dissociate from SOD to acquire more copper for subsequent cycles of chaperone copper loading and SOD metalation.

Heterodimer Model of LYS7−SOD Association and Copper Delivery. Due to the similarities between the LYS7 homodimer interface and the SOD homodimer interface, several laboratories have suggested that the most likely mode of copper delivery from LYS7 or hCCS to SOD1 occurs via a mechanism whereby a monomer of the copper chaperone for SOD forms a domain 2-mediated heterodimer with a monomer of SOD (18−20). Such a structural model generated by superimposing LYS7 domain 2 onto one of the subunits of yeast SOD reveals that the heterodimer interfaces are similar to both the SOD and LYS7 homodimeric interfaces with no critical steric interference between heterodimer interface residues (20). In this heterodimer model,
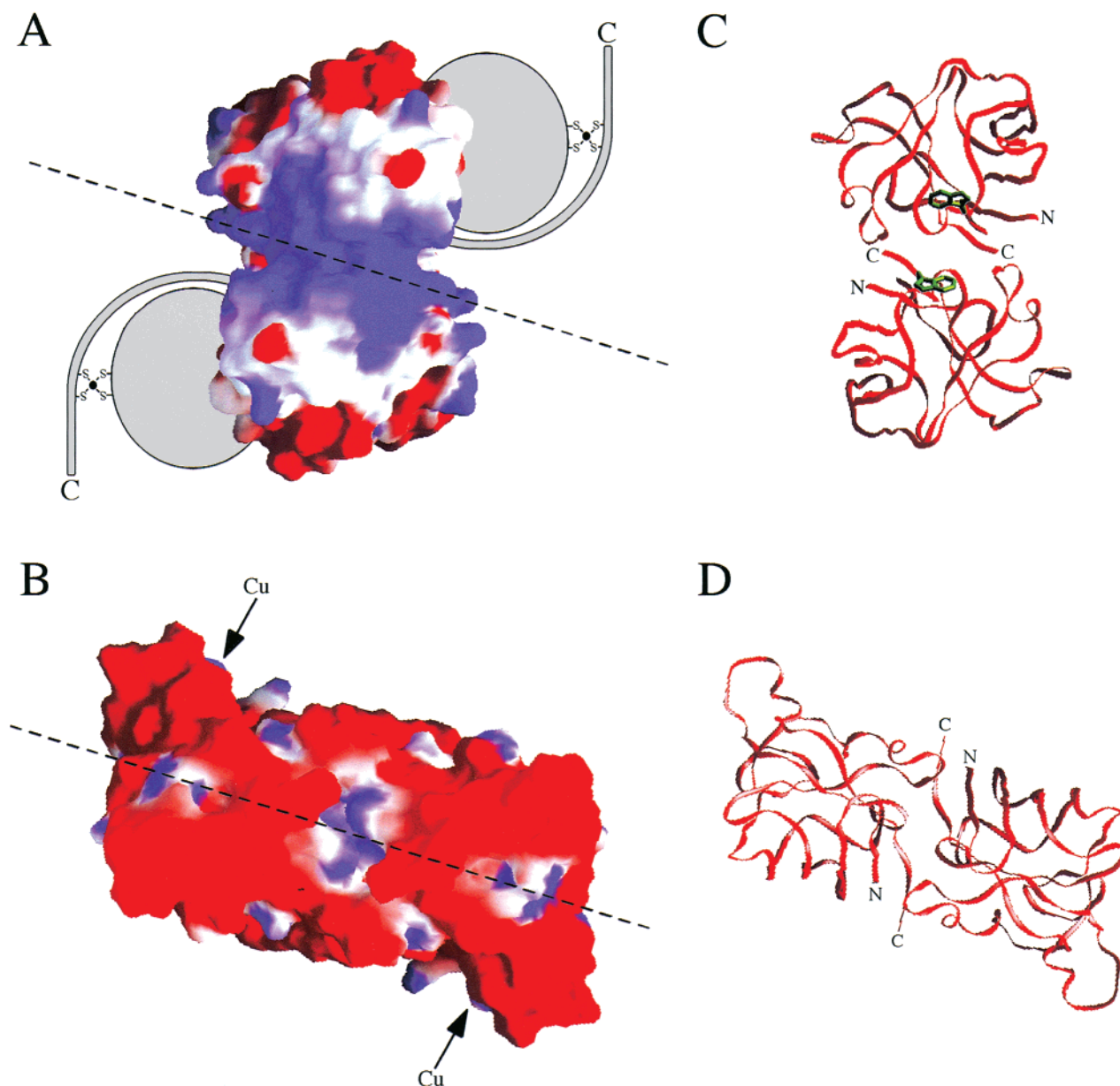
A

C

B

D

FIGURE 6: Dimer−dimer model of LYS7−SOD interaction and copper ion transfer. (A) Molecular surface map of the electrostatic potential of the L7D2 dimer calculated using GRASP (*33*). The blue and red contours calculated at ±2.5*kT*, respectively, represent positive and negative electrostatic potential. Domains 1 (N-terminal) and 3 (C-terminal) of LYS7 are represented as stylized circles and extended tails, respectively. The approximate positions of the putative copper binding sites in domains 1 and 3 of the LYS7 dimer are indicated. (B) Molecular surface map of the electrostatic potential of the yeast SOD homodimer calculated as described for panel A. The copper binding sites on yeast SOD are accessed in the plane of the paper as indicated by the arrows. The dashed lines represent the approximate orientation the yeast SOD dimer would assume upon docking with the LYS7 dimer. The yeast SOD surface shown is the putative docking surface, and the SOD molecule must be rotated by 180° around the dotted line for it to dock with the LYS7 dimer surface displayed here. Note that this 180° rotation puts the yeast SOD copper binding sites in position to face domains 1 and 3 of LYS7 such that their respective copper binding sites are in proximity. (C) Ribbon diagram of the L7D2 dimer in the same orientation as in panel A. The solvent-exposed symmetry-related Trp183 side chains of domain 2 are represented as green tube side chains. (D) Ribbon diagram of the yeast SOD homodimer in the same orientation as in panel B.

however, the metal binding region in the Atx1-like domain is approximately 40 Å from the copper binding site in SOD (*49*). Therefore, for direct copper transfer to occur via the Atx1-like domain, there must be substantial motion if it were to donate the copper to SOD (*49*).

Schmidt et al. (*18*) demonstrate that in LYS7 knockout yeast under conditions where copper is not limiting, LYS7 domains 2 and 3 alone are able to incorporate copper into apo-SOD, thereby rescuing the oxygen sensitive phenotype. In contrast, however, under limiting copper conditions, full-length LYS7 is required for copper insertion into apo-SOD

in vivo. Compelling evidence that domain 1 does indeed interact with domain 3 comes from the fact that it was found to act in trans with a truncated LYS7 molecule consisting of domains 2 and 3 alone under copper-limiting conditions (*18*). The importance of the domain 3 CXC motif in copper delivery is underscored by mutational studies that show that if either of the cysteines in this motif is converted to serine, copper transfer activity is severely diminished or lost even in the presence of the Atx1-like domain (*18*). The presence of the CXC motif for copper delivery to SOD therefore appears to be absolutely required.

Recently, a purely theoretical modeling study based on a monomer of the human copper chaperone for SOD (hCCS) forming a heterodimer with human SOD suggested that the flexible CXC motif in domain 3 can be positioned such that the CXC cysteine residues can coordinate copper held in the Atx1-like domain (domain 1) and then "swing" over to deposit copper into the vacant SOD copper binding site (*19*). This mode of copper delivery from the Atx1-like domain of hCCS to SOD would also require a very large movement of the C-terminal "copper delivery" domain (*19, 49*). We illustrate this concept in Figure 5 using a combination of the high-resolution crystal structures of L7D2 (this study) and yeast SOD (*39*) and stylistic rendering.

While this mode of copper ion delivery from the chaperone to SOD is attractive due to the similarities between the LYS7 and SOD dimer interfaces, a potentially serious flaw in this hypothesis is that SOD exists in many-fold excess relative to the copper chaperone in vivo (*47, 48*). This means that nascent yeast SOD, unless captured by a monomer of LYS7 immediately as it is translated, can form homodimers prior to receiving copper ion. The native SOD homodimer is extremely stable, and it seems unlikely that a monomer of LYS7 could effectively compete with and displace a monomer of SOD to perform its copper delivery function via the aforementioned heterodimer model. Furthermore, the very long and unstructured domain 3 of the LYS7 and hCCS molecules may be subject to proteolysis unless it is somehow protected or anchored, possibly by the MXCXXC motif of domain 1 or by direct interaction with SOD itself (see below). Taking these issues into account and because full-length LYS7 is predominantly dimeric when unreduced (Figure 2) or metal-loaded (*18*), we propose an alternative mode of chaperone−SOD interaction and copper delivery which obviates the rather serious problems that arise from the heterodimer model.

Dimer−Dimer Model of LYS7−SOD Association and Copper Delivery. Full-length LYS7 is dimeric in the crystal structure (*20*), under nonreducing conditions that may mimic the copper-loaded state in analytical ultracentrifugation studies (this study), and when metalated with copper in gel filtration studies (*18*). SOD also is a very tight homodimer (*49, 50*). These facts, coupled with the problems inherent in the heterodimer model of LYS7−SOD interaction and copper delivery described above (*49*), led us to search for an alternative mechanism of copper delivery to SOD that involves interaction of a dimer of LYS7 with a dimer of SOD. As a starting point for this analysis, we generated an L7D2 dimer by structurally aligning two molecules of our high-resolution L7D2 structure with the individual subunits of the yeast SOD homodimer, and looked for features that might suggest a surface that is able to interact with the SOD homodimer. We modeled Arg217 as glycine in our L7D2 crystal structure because its side chain was disordered. For the purposes of the following analysis, this side chain was introduced into the L7D2 homodimer in an extended conformation.

Careful inspection of the electrostatic surface potentials and structural features of the L7D2 homodimer, the SOD homodimer, and Figure 1 of the paper by Lamb et al. (*20*) immediately suggested a possible mechanism wherein a homodimer of LYS7 interacts with a homodimer of SOD in such a way that the symmetry-related domains 1 and 3 of

homodimeric LYS7 are close to the symmetry-related copper binding sites of homodimeric SOD. These features and the proposed dimer−dimer model of copper delivery are illustrated in Figure 6.

The L7D2 dimeric interface has a very electropositive nature relative to yeast SOD due to the substitution of charged residues for their hydrophobic counterparts, most notably, Lys136 and Arg217 in LYS7 for Phe50 and Leu151 in yeast SOD. As mentioned previously, these two substitutions translate into four local charge changes due to the 2-fold symmetry at the LYS7 dimer interface. These residues, with Arg188 (which is conserved in yeast SOD), are responsible for six solvent-exposed positive charges at the LYS7 dimer interface. It is also notable that Trp183 in LYS7 sits at the heart of the symmetrical dimer interface and is completely solvent-exposed. The symmetry-related Trp183 indole rings face each other (but are not within stacking distance) and appear poised for interaction with another protein, possibly via stacking interactions (Figure 6C).

The dimer−dimer model of LYS7−SOD interaction and copper delivery illustrated in Figure 6 can be summarized as follows. The positively charged LYS7 dimer interface (Figure 6A) with dual solvent-exposed tryptophan residues serves as the platform with which the predominantly negatively charged SOD dimer will interact (Figure 6B). The dotted lines running through the LYS7 and SOD dimers indicate the approximate orientation of the long axis of the SOD dimer when it is docked to LYS7. The negatively charged SOD electrostatic surface shown in Figure 6B is the putative docking surface, so the SOD molecule would therefore be rotated 180° around its dotted line before being placed on the positively charged LYS7 docking platform. This 180° SOD rotation and docking to LYS7 puts the copper binding sites of SOD very close to the MXCXXC metal binding site of domain 1 as well as to the CXC motif of domain 3 (represented stylistically) if they are associated in the copper delivery process. Under copper-limiting conditions, the CXC motif of domain 3 can acquire copper from the MXCXXC motif of domain 1 and, via a very small movement or conformational change, insert the copper ion into the high-affinity copper binding site of SOD. Domain 3, which is disordered in the full-length crystal structure of LYS7, could become ordered upon copper loading or upon interaction with SOD when the two dimers are docked. LYS7 domain 3−SOD contacts could be the "switch" that triggers copper movement from LYS7 to SOD. Once copper has been delivered to SOD, the allosteric changes described above and in ref *18* may facilitate either the loss of the LYS7 dimer or disruption of LYS7−SOD interactions so that the chaperone can recharge for another cycle of copper incorporation into SOD.

The advantages of the dimer−dimer model over the heterodimer model are several. (1) There is no need to disrupt the very stable SOD homodimer. (2) Instead of a 40 Å movement by either domain 1 or the CXC motif of domain 3 to the copper binding site of SOD, the distance would be much shorter, minimizing the possibility of copper loss. The movement of copper from lower (MXCXXC)- to higher-affinity sites (CuZnSOD) via domain 3 would occur in a very confined space and in a rapid time due to this proximity. (3) All biochemical data compiled to date are completely compatible with a dimer−dimer mechanism of LYS7−SOD

association and copper delivery. Although the dimer−dimer model has the above advantages over the heterodimer model of LYS7−SOD association and copper delivery, it should be stressed that both are possible. More experiments are necessary to delineate which of the two models (or some as yet undefined model) is ultimately correct.

CONCLUSIONS

We determined the three-dimensional structure of domain 2 of LYS7, the yeast copper chaperone for superoxide dismutase, and analyzed its solution behavior as well as that of the full-length apoprotein via analytical ultracentrifugation methods. Although L7D2 is monomeric both in the crystal and in solution, the full-length LYS7 molecule is dimeric in the crystal (*20*) and in a monomer−dimer equilibrium under nonreducing conditions in solution. Although the precise basis for the specificity of the LYS7−SOD interaction and the exact mechanism of copper insertion into SOD is unknown, it has been suggested that a monomer of LYS7 and a monomer of SOD associate to form a heterodimer via L7D2 and that copper is delivered to apo-SOD via domain 1 and/or domain 3 (*18−20*). While attractive, this model would necessitate disruption of the quite stable SOD homodimer. On the basis of (a) observations that full-length LYS7 can be dimeric in both crystalline and solution environments (ref *20* and this study), (b) features in the LYS7 structure that suggest a putative docking site for an SOD dimer with a LYS7 dimer, and (c) the spatial arrangement of the putative copper delivery domain(s) in the dimeric LYS7 structure (*20*), we suggest an alternative model for LYS7−SOD interaction and copper delivery that obviates the need to disrupt the very stable SOD homodimer and allows simultaneous copper ion delivery to both SOD subunits.

NOTE ADDED IN PROOF

Trp183 and Arg217, residues implicated in this study as being very important for the docking of yeast SOD to LYS7, are also found in a structurally equivalent position in the human CCS molecule. Recent data on metal binding to tomato and human CCS, using Co^{2+} as a spectroscopic probe, provide new evidence that the invariant Cys residues of domains 1 and 3 together are involved in metal coordination (*52*).

REFERENCES

1. Solomon, E. I., and Lowery, M. D. (1993) *Science 259*, 1575−1581.
2. Dancis, A., Haile, D., Yuan, D. S., and Klausner, R. D. (1994) *J. Biol. Chem. 269*, 25660−25667.
3. Culotta, V. C., Klomp, L. W. J., Strain, J., Casareno, R. L. B., Krems, B., and Gitlin, J. D. (1997) *J. Biol. Chem. 272*, 23469−23472.
4. Valentine, J. S., and Gralla, E. B. (1997) *Science 278*, 817−818.
5. Glerum, D. M., Shtanko, A., and Tzagoloff, A. (1996) *J. Biol. Chem. 271*, 14504−14509.
6. Srinavasan, C., Posewitz, M. C., George, G. N., and Winge, D. R. (1998) *Biochemistry 37*, 7572−7577.
7. Pufahl, R. A., Singer, C. P., Peariso, K. L., Lin, S., Schmidt, P. J., Fahrni, C. J., Culotta, V. C., Penner-Hahn, J. E., and O'Halloran, T. V. (1997) *Science 278*, 853−856.
8. Lin, S. J., Pufahl, R. A., Dancis, A., O'Halloran, T. V., and Culotta, V. C. (1997) *J. Biol. Chem. 272*, 9215−9220.
9. Rosen, D. R., Siddique, T., Patterson, D., Figlewicz, D. A., Sapp, P., Hentati, A., Donaldson, D., Goto, J., O'Regan, J. P., Deng, H. X., Rahmani, Z., Krizus, A., McKenna-Yasek, D., Cayabyab, A., Gaston, S. M., Berger, R., Tanzi, R. E., Halperin, J. J., Herzfeldt, B., Van den Bergh, R., Hung, W. Y., Bird, T., Deng, G., Mulder, D. W., Smyth, C., Laing, N. G., Soriano, E., Pericak-Vance, M. A., Haines, J., Rouleau, G. A., Gusella, J. S., Horvitz, H. R., and Brown, R. H. (1993) *Nature 362*, 59−62.
10. Wiedau-Pazos, M., Goto, J. J., Rabizadeh, S., Gralla, E. B., Roe, J. A., Lee, M. K., Valentine, J. S., and Bredesen, D. E. (1996) *Science 271*, 515−518.
11. Yim, M. B., Kang, J. H., Yim, H. S., Kwak, H. S., Chock, P. B., and Stadtman, E. R. (1996) *Proc. Natl. Acad. Sci. U.S.A. 93*, 5709−5714.
12. Lyons, T. J., Nersissian, A. M., Goto, J. J., Zhu, H., Gralla, E. B., and Valentine, J. S. (1998) *J. Biol. Inorg. Chem. 3*, 650−662.
13. Lutsenko, S., and Kaplan, J. H. (1995) *Biochemistry 34*, 15607−15613.
14. Solioz, M., and Vulpe, C. (1996) *Trends Biochem. Sci. 21*, 237−241.
15. Lin, S. J., and Culotta, V. C. (1995) *Proc. Natl. Acad. Sci. U.S.A. 92*, 3784−3788.
16. Rosenzweig, A. C., Huffman, D. L., Hou, M. Y., Wernimont, A. K., Pufahl, R. A., and O'Halloran, T. V. (1999) *Structure 7*, 605−617.
17. Casareno, R. L. B., Waggoner, D., and Gitlin, J. D. (1998) *J. Biol. Chem. 273*, 23625−23628.
18. Schmidt, P. J., Rae, T. D., Pufahl, R. A., Hamma, T., Strain, J., O'Halloran, T. V, and Culotta, V. C. (1999) *J. Biol. Chem. 274*, 23719−23725.
19. Falconi, M., Iovino, M., and Desideri, A. (1999) *Structure 7*, 903−908.
20. Lamb, A. L., Wernimont, A. K., Pufahl, R. A., Culotta, V. C., O'Hallloran, T. V., and Rosenzweig, A. C. (1999) *Nat. Struct. Biol. 6*, 724−729.
21. Horecka, J., Kinsey, P. T., and Sprague, G. F., Jr. (1995) *Gene 162*, 87−92.
22. Studier, F. W., Rosenberg, A. H., Dunn, J. J., and Dubendorff, J. W. (1990) *Methods Enzymol 185*, 60−89.
23. Nersissian, A. M., Mehrabian, Z. B., Nalbandyan, R. M., Hart, P. J., Fraczkiewicz, G., Czernuszewicz, R. S., Bender, C. J., Peisach, J., Herrmann, R. G., and Valentine, J. S. (1996) *Protein Sci. 5*, 2184−2192.
24. Terwilliger, T. C., and Bredezen, J. (1999) *Acta Crystallogr. D55*, 849−861.
25. LaFortelle, E., and de Bricogne, G. (1997) *Methods Enzymol. 276*, 472−494.
26. Collaborative Computational Project, Number 4 (1994) *Acta Crystallogr. D50*, 760−763.
27. Brunger, A. T. (1988) in *Crystallographic computing 4: Techniques and new technologies* (Isaacs, N. W., and Taylor, M. R., Eds.) pp 126−140, Clarendon Press, Oxford, U.K.
28. Sheldrick, G. M., and Schneider, T. R. (1997) *Methods Enzymol. 277*, 319−343.
29. Jones, T. A., Zou, J. Y., Cowan, S. W., and Kjeldgaard, M. (1991) *Acta Crystallogr. A47*, 110−119.
30. Hodel, A., Kim, S. H., and Brünger, A. T. (1992) *Acta Crystallogr. A48*, 851−858.
31. Satow, Y., Cohen, G. H., Padlan, E. A., and Davies, D. R. (1986) *J. Mol. Biol. 190*, 593−604.
32. Evans, S. V. (1993) *J. Mol. Graphics 11*, 134−138.
33. Nicholls, A., Sharp, K. A., and Honig, B. (1991) *Proteins 11*, 281−296.
34. van Holde, K. E., and Weischet, W. O. (1978) *Biopolymers 17*, 1387−1403.
35. Demeler, B., Saber, H., and Hansen, J. C. (1997) *Biophys. J. 72*, 397−407.

36. Johnson, M. L., Correia, J. J., Yphantis, D. A., and Halvorson, H. R. (1981) *Biophys. J. 36*, 575−588.
37. Read, R. J. (1986) *Acta Crystallogr. A42*, 140−149.
38. Ramachandran, G. N., and Sasiskharam, V. (1968) *Adv. Protein Chem. 23*, 283−437.
39. Ogihara, N. L., Parge, H. E., Hart, P. J., Weiss, M. S., Goto, J. J., Crane, B. R., Tsang, J., Slater, K., Roe, J. A., Valentine, J. S., Eisenberg, D., and Tainer, J. A. (1996) *Biochemistry 35*, 2316−2321.
40. Tainer, J. A., Getzoff, E. D., Beem, K. M., Richardson, J. S., and Richardson, D. C. (1982) *J. Mol. Biol. 160*, 181−217.
41. Deng, H. X., Hentati, A., Tainer, J. A., Iqbal, Z., Cayabyab, A., Hung, W. Y., Getzoff, E. D., Hu, P., Herzfeldt, B., Roos, R. P., Warner, C., Deng, G., Soriano, E., Smyth, C., Parge, H. E., Ahmed, A., Roses, A. D., Hallewell, R. A., Pericak-Vance, M. A., and Siddique, T. (1993) *Science 261*, 1047−1051.
42. Hart, P. J., Liu, H., Pellegrini, M., Nersissian, A. M., Gralla, E. B., Valentine, J. S., and Eisenberg, D. (1998) *Protein Sci. 7*, 545−555.
43. Bertini, I., Piccioli, M., Viezzoli, M. S., Chiu, C. Y., and Mullenbach, G. T. (1994) *Eur. J. Biophys. 23*, 167−176.
44. Cole, J. L., and Hansen, J. C. (1999) *J. Biomol. Technol.* (in press).
45. Hansen, J. C., Lebowitz, J., and Demeler, B. (1994) *Biochemistry 33*, 13155−13163.
46. Bernstein, F. C., Koetzle, T. F., Williams, G. J., Meyer, E. E., Brice, M. D., Rodgers, J. R., Kennard, O., Shimanouchi, T., and Tasumi, M. (1977) *J. Mol. Biol. 112*, 535−542.
47. Rae, T. D., Schmidt, P. J., Pufahl, R. A., Culotta, V. C., and O'Halloran, T. V. (1999) *Science 284*, 805−808.
48. Rothstein, J. D., Dykes-Hoberg, M., Corson, L. B., Becker, M., Cleveland, D. W., Price, D. L., Culottta, V. C., and Wong, P. C. (1999) *J. Neurochem. 72*, 422−429.
49. Poulos, T. L. (1999) *Nat. Struct. Biol. 6*, 709−711.
50. Valentine, J. S., and Pantoliano, M. W. (1981) in *Copper Proteins* (Spiro, T. G., Ed.) pp 291−358, Wiley-Interscience, New York.
51. Otwinowski, Z., and Minor, W. (1997) *Methods Enzyumol. 276*, 307−326.
52. Zhu, H., Shipp, E., Sanchez, R. J., Liba, A., Stine, J. E., Hart, P. J., Gralla, E. B., Nersissian, A. M., and Valentine, J. S. (2000) Cobalt(2+) binding to human and tomato copper chaperone for superoxide dismutase. Implication for the metal ion transfer mechanism, *Biochemistry* (in press).